

## Article

# Synthesis of Hollow Leaf-Shaped Iron-Doped Nickel–Cobalt Layered Double Hydroxides Using Two-Dimensional (2D) Zeolitic Imidazolate Framework Catalyzing Oxygen Evolution Reaction

Quoc Hao Nguyen , Kyungmin Im \* and Jinsoo Kim \*

Department of Chemical Engineering (Integrated Engineering), Kyung Hee University, 1732 Deogyong-daero, Giheung-gu, Yongin-si 17104, Gyeonggi-do, Republic of Korea

\* Correspondence: catt917@khu.ac.kr (K.I.); jkim21@khu.ac.kr (J.K.)

**Abstract:** Layered double hydroxides (LDHs) have been reported as one of the most effective materials for oxygen evolution reaction (OER) catalysts, which are prone to hydrolysis and oxidation under OER conditions. Metal–organic frameworks (MOFs) are porous materials with high crystallinity and internal surface area. The design of LDHs based on MOFs has attracted increasing attention owing to their high surface area, exposed catalysis sites, and fast charge/mass transport kinetics. Herein, we report a novel approach to fabricate a leaf-shaped iron-doped nickel–cobalt LDH (L-Fe-NiCoLDH) derived from a two-dimensional (2D) zeolitic imidazolate framework with a leaf-like morphology (ZIFL). Iron doping played a significant role in enhancing the specific surface area, affecting the OER performance. L-Fe-NiCoLDH showed high OER performance with an overpotential of 243 mV at 10 mA cm<sup>-2</sup> and high durability after 20 h. The design of LDHs based on the leaf morphology of MOFs offers tremendous potential for improving OER efficiency.

**Keywords:** Layered double hydroxides; leaf shape; metal–organic framework; nonprecious metal hydroxides; oxygen evolution reaction



**Citation:** Nguyen, Q.H.; Im, K.; Kim, J. Synthesis of Hollow Leaf-Shaped Iron-Doped Nickel–Cobalt Layered Double Hydroxides Using Two-Dimensional (2D) Zeolitic Imidazolate Framework Catalyzing Oxygen Evolution Reaction. *Catalysts* **2023**, *13*, 403. <https://doi.org/10.3390/catal13020403>

Academic Editors: Kyubock Lee and Min-Jae Kim

Received: 13 January 2023

Revised: 10 February 2023

Accepted: 11 February 2023

Published: 14 February 2023



**Copyright:** © 2023 by the authors. Licensee MDPI, Basel, Switzerland. This article is an open access article distributed under the terms and conditions of the Creative Commons Attribution (CC BY) license (<https://creativecommons.org/licenses/by/4.0/>).

## 1. Introduction

Energy and the environment are among the essential concerns of the present age [1]. The global demand for energy consumption is increasing, along with the problems associated with global warming and the rapid depletion of fossil fuels [2]. Therefore, converting and storing energy from renewable sources is an encouraging solution to reduce fossil fuel dependence significantly [3]. Among the various energy systems, fuel cells, metal–air batteries, and water splitting have been identified as the most impressive and efficient methods for addressing the issues above [4]. The oxygen evolution reaction (OER) plays an important role in many electrochemical reactions, including the production of hydrogen in zinc–air batteries [5–7]. The OER is a slow reaction, and a large potential must be applied to overcome the reaction barrier and achieve a high reaction rate, leading to the catalysts in use today that often require very expensive materials, such as precious metal oxides (e.g., IrO<sub>2</sub> and RuO<sub>2</sub>) [8]. As a substitute for precious metal oxides, perovskite-type oxide structures [9,10], spinel-type oxides [11,12], amorphous metal oxides [13], and layered double hydroxides (LDHs) [14,15] based on 3D transition metals have been reported, but they have yet to show high performance along with durability [16].

Among them, the design of LDHs has attracted attention owing to their two-dimensional (2D) structure with abundant metal hydroxide (M(OH); M = Fe, Co, Ni, Mn, etc.) active sites for rapid electrochemical redox reactions [17]. Recently, Fe, Co, and Ni compounds have been discovered to be the best catalysts for the OER. In particular, Ni- and Co-based LDHs can offer the synergistic effects of Ni and Co. Mechanical studies showed that the

oxidation of  $\text{Co}^{2+}$  and  $\text{Ni}^{2+}$  into  $\text{Co-OOH}$  or  $\text{Ni-OOH}$  provided active sites for the OER process, but it also caused poor electrical conductivity and electronic stability [18]. Although Ni- and Fe-based LDHs offer large performance, Fe-, Ni-, and Co-mixed metal oxides exhibit even more enhanced performance [19]. Nocera et al. suggested that small amounts of  $\text{Fe}^{3+}$  influenced the formation of highly valence nickel states in LDHs, enhancing beneficial oxyl characteristics and thereby improving OER activity [20]. Furthermore, Fe has an ionic radius similar to a Ni or Co cation, facilitating its substitution into Ni and Co positions. Markovic et al. reported a tendency of high and stable activity for  $\text{Fe-MO}_x\text{H}_y$  based on dissolution and repositioning at the surface of the electrolyte/object, improving the performance and stability of the OER [21]. Mixed metal oxides can optimize the adsorption energy of catalysts and increase the electrical conductivity of catalysts to improve efficiency and stability, further reducing the usable metal content to maintain catalyst activity.

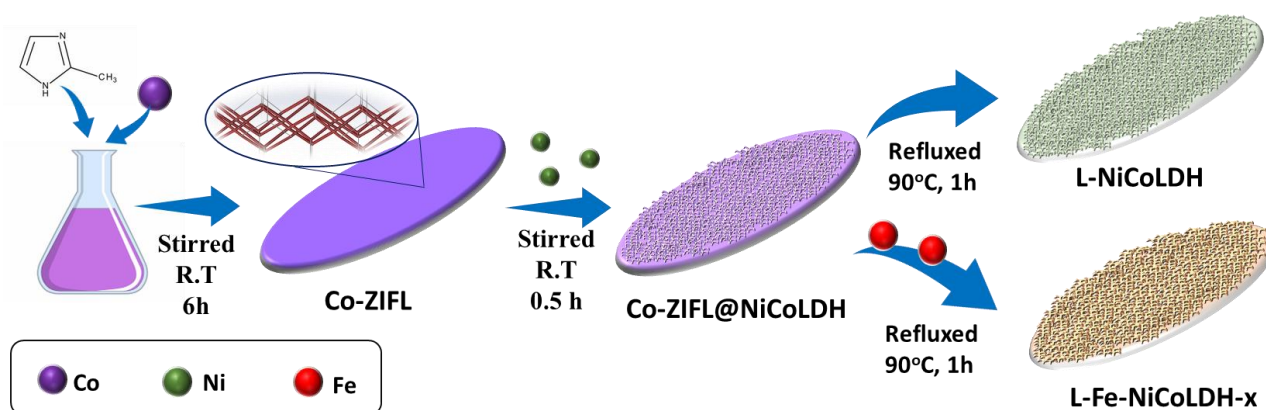
Metal–organic frameworks (MOFs) are porous materials with high crystallinity and large internal surface area, formed by coordinated bonds of metal ions/clusters and organic ligands [22–24]. Based on their characteristics, MOF-derived materials are used as templates or metal sources of electrocatalysts in fuel cells, zinc–air batteries, and water splitting [25–27]. Specifically, the use of MOFs as sacrificial templates for LDHs or metal oxide/sulfide/hydroxide had high OER performance [28]. York-shell [29], core–shell [30,31], hollow [32,33], and ultrathin MOFs [34,35] have been considered suitable precursors for fabricating catalysts for high OER performance.

In this work, we report a novel and simple method to synthesize a hollow and porous Fe-doped NiCoLDH based on the leaf morphology of a MOF. This strategy involves the construction of leaf-shaped cobalt zeolitic imidazolate frameworks (Co-ZIFL) and ion exchange and etching processes with  $\text{Ni}(\text{NO}_3)_2$  in ethanol, followed by refluxing in the presence of  $\text{Fe}(\text{NO}_3)_3$  in an oil bath. The optimum Fe incorporation enabled the synthesis of LDH structures and increased their specific surface area, thereby improving the OER performance. The design of nanostructures such as LDHs based on the leaf morphology of MOFs can significantly enhance OER efficiency.

## 2. Results and Discussion

Scheme 1 shows the synthesis process of all L-Fe-NiCoLDH-x and L-NiCoLDH samples. First, the Co-ZIFL precursor was fabricated by mixing cobalt nitrate and 2-methylimidazole in water. Figure S1a,b shows the leaf-like morphology of Co-ZIFL. The crystal structure of Co-ZIFL was examined by XRD, which is consistent with the simulated ZIFL patterns (Figures 1a and S2a). When Co-ZIFL was added to a nickel nitrate solution, the protonated  $\text{Ni}^{2+}$  in nickel nitrate etched the Co-ZIFL. At this time,  $\text{Co}^{2+}$  cations were released from the ZIF, and they coprecipitated with hydroxy ions on the leaf surface to create an LDH structure [36,37]. The XRD pattern of Co-ZIFL@NiCoLDH maintained the main peaks of Co-ZIFL and showed a new broader peak at  $10.9^\circ$ , indicating the formation of an LDH structure. After refluxing, the L-NiCoLDH sample showed peaks at  $10.9^\circ$ ,  $22.1^\circ$ ,  $33.5^\circ$ , and  $60.3^\circ$  corresponding to the (003), (006), (112), and (110) planes of the typical LDH structure, respectively, as shown in Figure 1a. Similar XRD patterns were observed in the L-Fe-NiCoLDH-x samples (Figures 1a and S2b), indicating that the LDH structure was maintained upon the intercalation of  $\text{Fe}^{3+}$  cations.

The effects of the refluxing step on synthesized LDH structures were examined by Fourier-transform infrared spectroscopy (FTIR), as shown in Figure 1b. The FTIR spectrum of Co-ZIFL@NiCoLDH involved Co-ZIFL peaks, indicating that the ZIF structure was maintained after the reaction for 0.5 h. After the refluxing step at  $90^\circ\text{C}$  for 1 h, the FTIR spectrum of L-Fe-NiCoLDH-x did not show any peaks related to the ZIF structure and showed new peaks assigned to the LDH structure at  $3497\text{ cm}^{-1}$  (hydroxyl groups),  $1629\text{ cm}^{-1}$  (interlayer water molecules),  $1339\text{ cm}^{-1}$  (the stretching of the interlayer carbonate anion),  $1053\text{ cm}^{-1}$  (the stretching of the interlayer carbonate anion), and  $649\text{ cm}^{-1}$  (the vibration of M–O bonds) [38].



Scheme 1. Synthesis process of L-Fe-NiCoLDH-x and L-NiCoLDH.

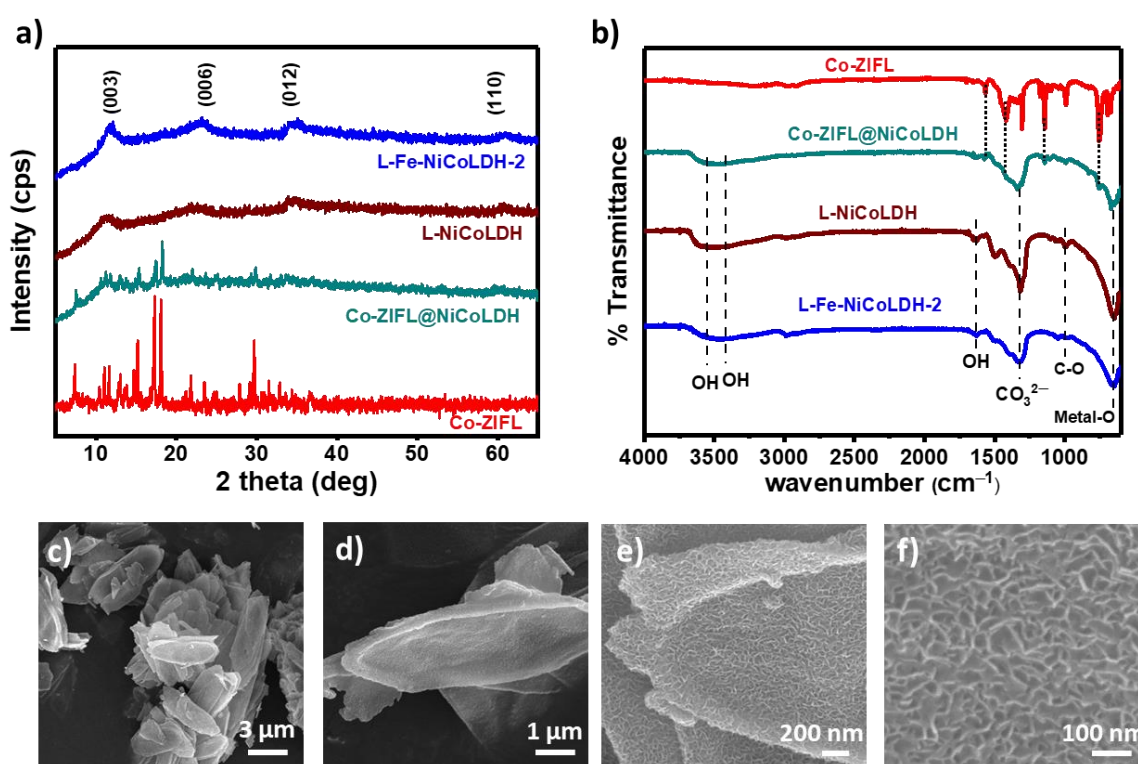
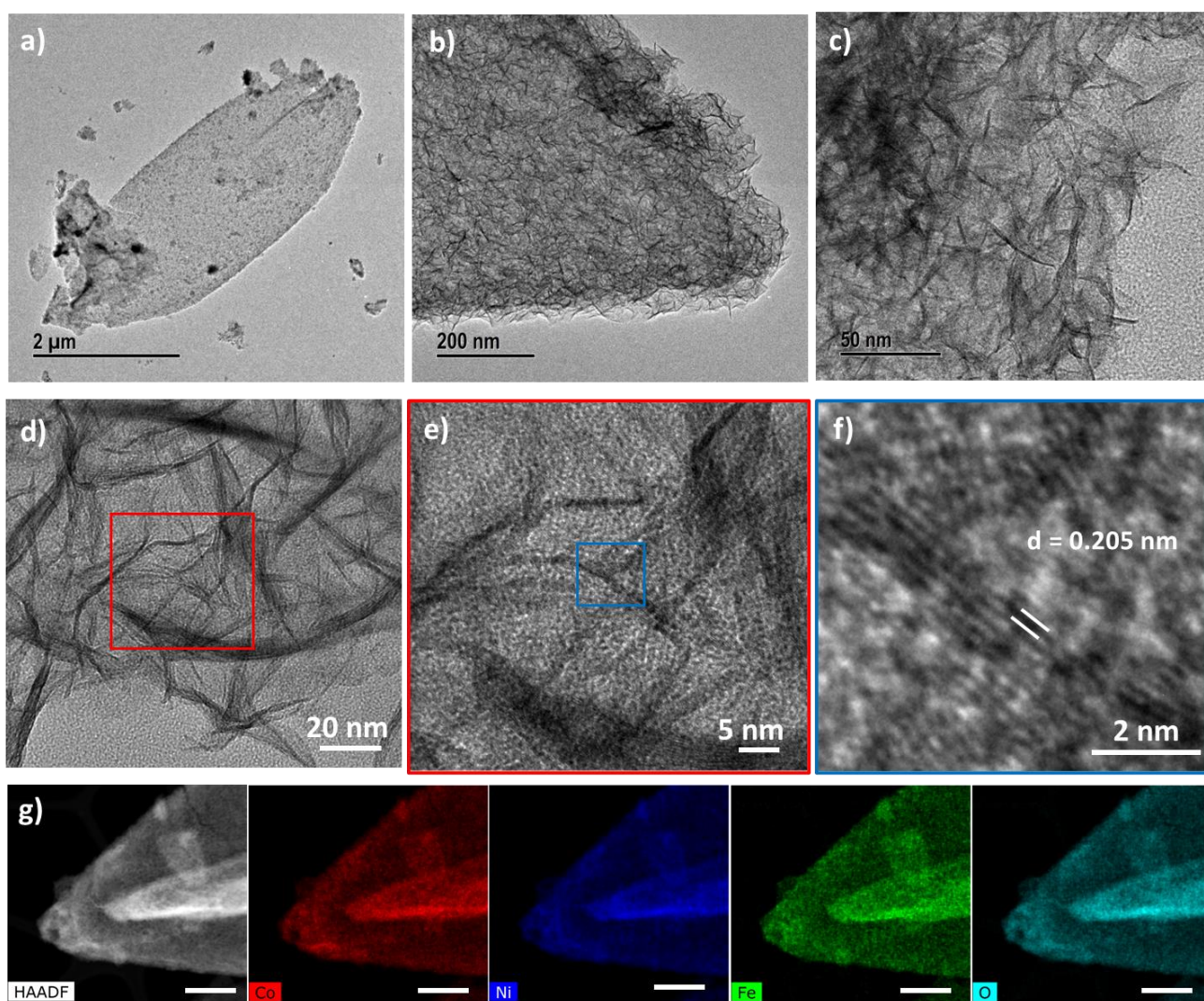


Figure 1. (a) XRD patterns and (b) FTIR spectra of Co-ZIFL, Co-ZIFL@NiCoLDH, L-NiCoLDH and L-Fe-NiCoLDH-2. (c–f) SEM images of L-Fe-NiCoLDH-2.

The morphology of L-Fe-NiCoLDH-2 is shown in Figure 1c–f. Although it maintained the leaf shape of Co-ZIFL, which acted as a template, some structures were broken. In addition, changes in surface morphology after LDH structural transformation were indicated by nanoflakes around leaf-like structures similar to those observed for L-NiCoLDH (see Figure S3a,b). In particular, the Fe concentration affected the morphology of the catalyst. The morphology of L-Fe-NiCoLDH-1 was maintained, as shown in Figure S3c,d. However, the morphology of L-Fe-NiCoLDH-3 using high  $\text{Fe}^{3+}$  concentration was almost completely broken, as shown in Figure S3e,f.

The morphology of L-Fe-NiCoLDH-2 and L-NiCoLDH was further characterized by FE-TEM, as shown in Figures 2a–c and S4. Although the whole leaf shape was maintained, the structure changed to a hollow leaf completely covered with nanoflakes. At high magnification (Figure 2c,d), nanoflakes covering the leaves were observed. From the high-resolution FE-TEM (HR) images (Figures 2e–f and S4d), the interlayer spacing between

lattice fringes of L-Fe-NiCo-LDH-2 is 0.205 nm, which is smaller than that of L-NiCoLDH sample (0.271 nm). The results demonstrate the successful doping of iron in the LDH structure, leading to a change in the crystal structure. EDX mapping was analyzed to demonstrate the presence of Fe, Co, Ni, and O species in the L-Fe-NiCoLDH-2 catalyst, as shown in Figure 2g. The elements of Fe, Ni, Co, and O were well dispersed throughout the leaf, demonstrating the homogeneity of the developed LDH structure. Further, the EDX mapping results of L-NiCoLDH showed that the elements of Ni, Co, and O species were well dispersed (Figure S5). The EDX results of all L-Fe-NiCoLDH- $x$  ( $x = 1, 2, 3$ ) samples are shown in Figure S6, and their metal compositions are shown in Table S1. The metal ratios of Ni to Co were similar in all samples. Specifically, the proportion of Fe increased as the added Fe amount increased, indicating the successful doping of Fe in the refluxing step.



**Figure 2.** (a–c) FE-TEM images, (d–f) HR-TEM images, and (g) HAADF and EDX mapping images of L-Fe-NiCoLDH-2 (scale bar is 400 nm).

The electrochemical performances of the catalysts are significantly affected by the pore structure and the specific surface area. Figure 3a shows the nitrogen adsorption/desorption isotherms of the L-NiCoLDH and L-Fe-NiCoLDH- $x$  samples. All catalysts showed hysteresis loops, indicating the presence of mesoporous structures. In particular, L-Fe-NiCoLDH-2 showed the highest specific surface area ( $159.85 \text{ m}^2 \text{ g}^{-1}$ ). As shown in Table 1, the addition of Fe increased the specific surface areas significantly, which is explained by the change in the layer spacing of LDH upon Fe doping [39]. Figure 3b shows the pore size distributions of the L-NiCoLDH and L-Fe-NiCoLDH- $x$  samples, indicating a higher mesoporous volume

of L-Fe-NiCoLDH-2. Owing to the developed mesopore structure and high specific surface area, electron transport can be facilitated between the electrolyte and active sites.

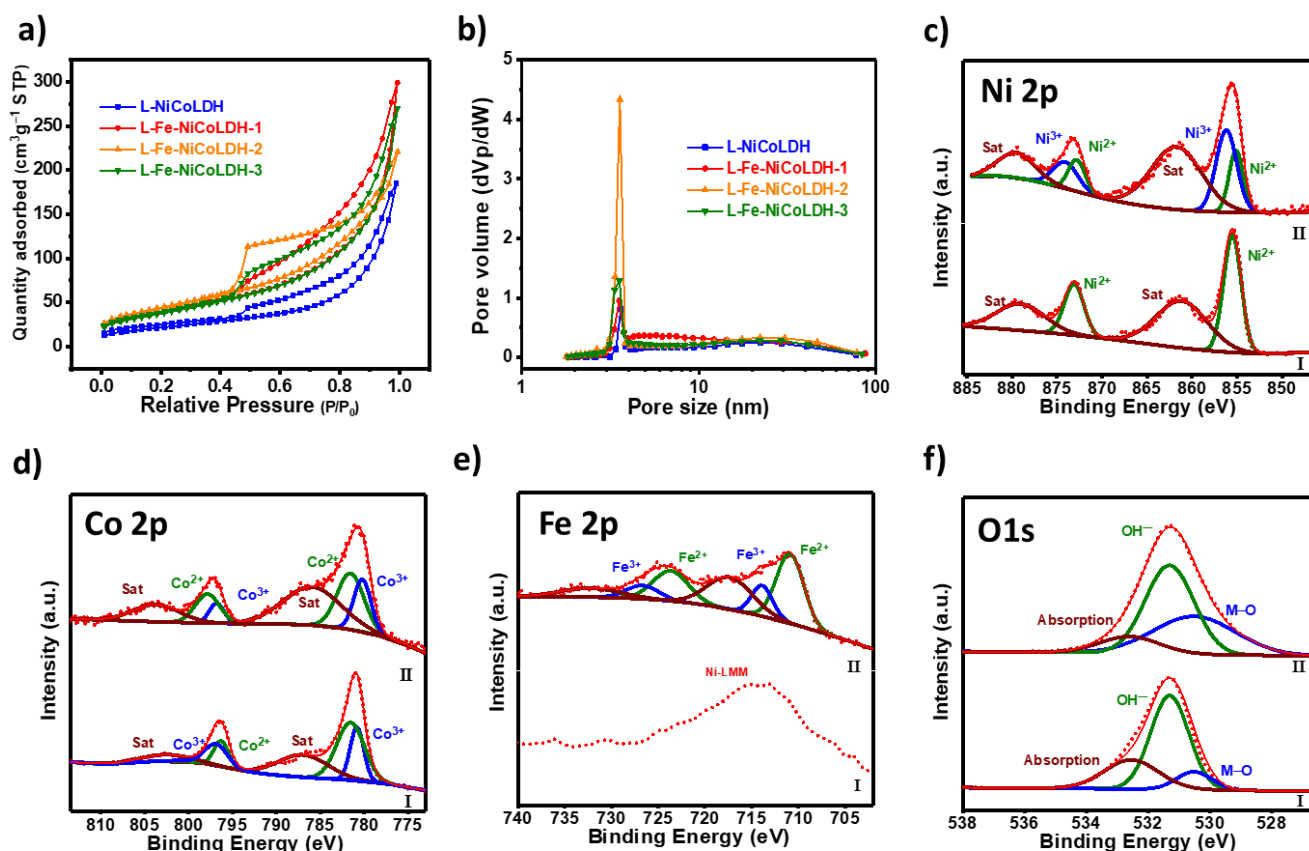


**Figure 3.** (a) Nitrogen isotherm curves and (b) BJH plots of L-NiCo-LDH and L-FeNiCo-LDH-x. High-resolution XPS spectra of (I) L-NiCoLDH and (II) L-Fe-NiCoLDH-2: (c) Ni 2p, (d) Co 2p, (e) Fe 2p, and (f) O 1s.

**Table 1.** Summary of the surface area and pore size analysis of the catalysts.

Sample	Surface Area (m <sup>2</sup> g <sup>-1</sup> )	Pore Size (nm)	Total Pore Volume (cm <sup>3</sup> g <sup>-1</sup> )
L-NiCo LDH	78.66	6.41	0.13
L-Fe-NiCoLDH-1	140.23	5.67	0.21
L-Fe-NiCoLDH-2	159.85	5.29	0.22
L-Fe-NiCoLDH-3	137.53	5.68	0.21

The surface compositions and oxidation states of the elements were investigated by XPS. The survey spectrum showed the peaks of Ni, Co, Fe, and O elements, as shown in Figure S7, and the surface atomic concentrations showed in Table S2. The clear signal for Fe 2p in XPS of L-Fe-NiCoLDH-2 further demonstrates that Fe has been decorated on the LDH structure. In Figure 3c, Ni 2P peaks appeared at 855.1 eV and 872.8 eV attributed to peak of Ni<sup>2+</sup>, and 856.1 and 874.1 eV attributed to peak of Ni<sup>3+</sup> [40]. In addition, two satellite peaks were observed at 861.7 eV and 874.1 eV, which corresponded to  $\gamma$ -NiOOH, which is believed to enhance OER performance [41]. For comparison, the Ni 2p of L-NiCoLDH showed prominent peaks at 855.9 and 873.2 eV corresponding to Ni<sup>2+</sup> only. These results show the effect of Fe on the oxidation of Ni<sup>2+</sup> to Ni<sup>3+</sup>. The high-resolution Co 2p spectra of L-NiCoLDH and L-Fe-NiCoLDH-2 are shown in Figure 3d. Two groups of peaks attributed to Co<sup>2+</sup> and Co<sup>3+</sup> were fitted at 781.0 eV/796.3 eV and 779.7/795.3 eV, respectively, and satellite peaks appeared at 785.1 eV and 801.8 eV [42,43]. The high-resolution analysis of the Co 2p spectra of L-NiCoLDH and L-Fe-NiCoLDH-2 showed no noticeable difference,

confirming that  $\text{Fe}^{3+}$  affected only the oxidation state of Ni. The Auger peak of the Ni LMM interfered with the high-resolution Fe 2p spectrum of L-NiCoLDH, where the  $\text{Fe}^{2+}$  and  $\text{Fe}^{3+}$  peaks appeared at 711.1/723.8 eV and 714.0/726.9 eV, respectively (Figure 3e) [44–46]. The high-resolution O 1s spectrum in Figure 3f can be deconvoluted into three peaks. The peak at 530.5 eV was assigned to the metal–oxygen bond, the peak at 531.3 eV was assigned to OH in the LDH structure, and the last peak at 532.5 eV originated from oxygen adsorption [47,48].

The oxygen evolution reaction performance of all catalysts was studied in an alkaline electrolyte (1 M KOH). Figure 4a shows the linear sweep voltammetry (LSV) curves of the L-Fe-NiCoLDH-x and L-NiCoLDH catalysts. All samples showed redox peaks from 1.25 to 1.35 V vs. RHE owing to the preoxidation of metal ions to higher oxidation states [49]. As the amount of  $\text{Fe}^{3+}$  increased, the oxidant peak became more positive, suggesting the modification of the electronic structure of the catalyst. Moreover, these changes can enhance the overall OER activity of the catalyst by increasing the conductivity [50,51].

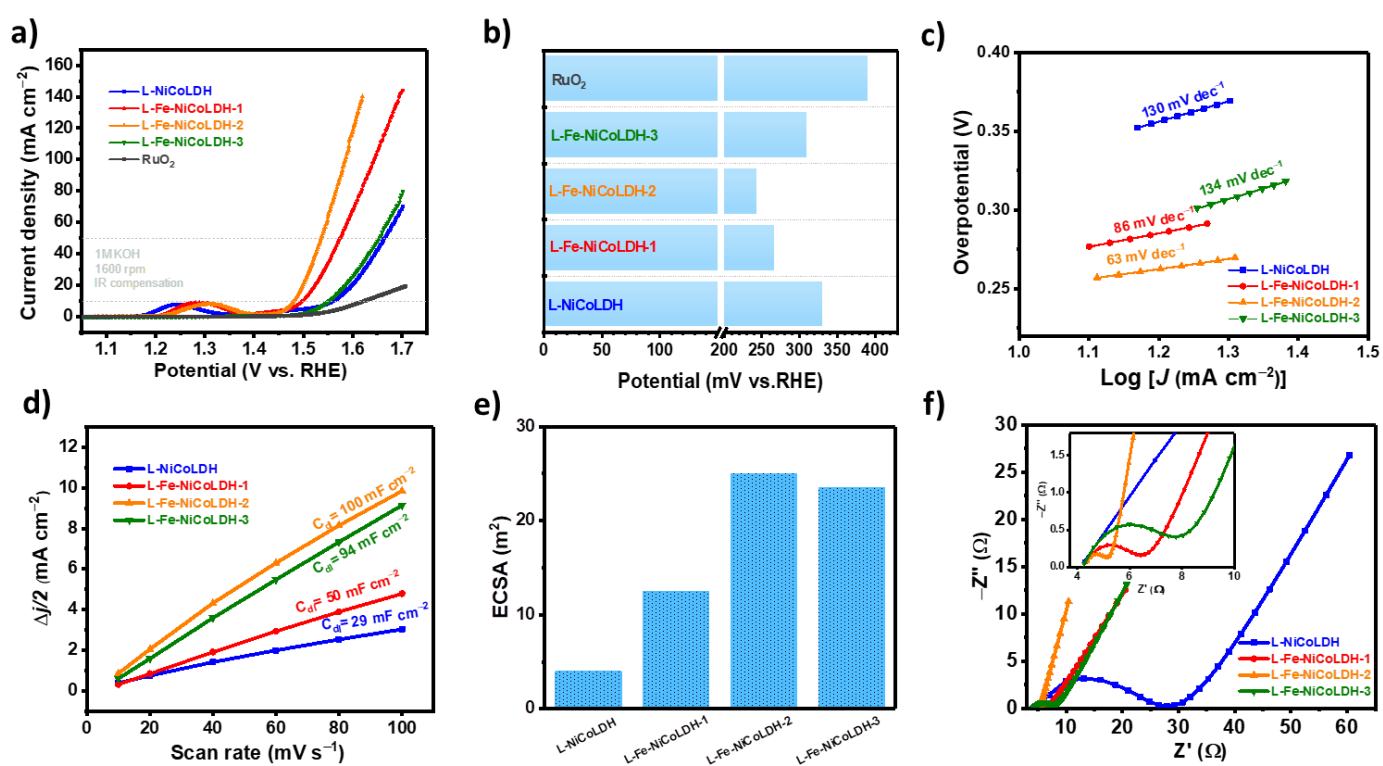


**Figure 4.** Oxygen evolution reaction in 1 M KOH. (a) LSV curves of catalysts scanned at  $5 \text{ mV s}^{-1}$  from 1.05 V to 1.7 V. (b) Overpotential of catalysts at  $10 \text{ mA cm}^{-2}$ . (c) Tafel slope of catalysts obtained from LSV curves. (d) Double-layer capacitance as a function of CV scan rates. (e) the electrochemically active surface area calculated from double-layer capacitance (f) Nyquist plots (the inset is the enlarged plot of the selected area) of catalysts.

The overpotentials of the catalysts were compared at  $10 \text{ mA cm}^{-2}$ , as shown in Figure 4b. The lowest overpotential (243 mV vs. RHE) was measured for L-FeNiCoLDH-2. The overpotentials of 331 mV, 267 mV, 309 mV, and 390 mV vs. RHE were obtained for L-NiCoLDH, L-Fe-NiCoLDH-1, L-Fe-NiCoLDH-3, and commercial  $\text{RuO}_2$ , respectively. Tafel curves were calculated from the LSV curves to gain further insights into the OER kinetics of the catalysts, as shown in Figure 4c. L-Fe-NiCoLDH-2 exhibited the lowest Tafel slope of  $63 \text{ mV dec}^{-1}$ , while L-Fe-NiCoLDH-1, L-Fe-NiCoLDH-3, and L-NiCoLDH exhibited Tafel slopes of 86, 134, and  $130 \text{ mV dec}^{-1}$ , respectively. The OER performances and Tafel slopes were also compared with those of the LDH catalysts reported in the literature (see Table 2).

**Table 2.** Comparison of the electrocatalytic properties of the as-prepared L-Fe-NiCoLDH toward the OER with previously reported catalysts (Electrolyte: KOH 1 M).

Number	Catalyst	Overpotential ( $\eta_{10}$ ) [mV]	Tafel Slope [mV dec <sup>-1</sup> ]	Ref
1	L-FeNiCoLDH-2	243	63	This work
2	etched-CoFe-LDH	302	41	[52]
3	MnCo-LDH/graphene	330	48	[53]
4	NiCo LDH@ZIF-67-V <sub>O</sub> /NF	290	58	[43]
5	(Co,Ni)Se <sub>2</sub> @NiFe LDH	277	75	[33]
6	(Ru-Co)O <sub>x</sub> -350	265	60	[54]
7	TCO <sub>2</sub> P@C	328	57	[55]
8	Br-Ni-MOF(A)	306	79.1	[56]
9	NiFe-25	299	48.7	[57]
10	NiCo <sub>2</sub> O <sub>4</sub> @MoS <sub>2</sub> /TM	313	66.8	[58]

To gain an in-depth understanding of the OER performance, the ECSA and charge transfer resistance ( $R_{ct}$ ) were studied. The ECSA was investigated by checking the electrochemical double-layer capacitance ( $C_{dl}$ ), which was obtained via the CV cycle in the non-faradaic region. The CV cycles of L-Fe-NiCoLDH-2 and other catalysts were performed in the potential range from 1.3 to 1.5 V vs. RHE in 1 M KOH with scan rates of 10, 20, 40, 60, 80, and 100 mV s<sup>-1</sup> (see Figure S8). The CV curves of the catalysts in this potential range showed the typical geometry of a double-layer capacitor, indicating that the electrode reaction of the charge is negligible and that the current response was collected from the charge and discharge process of the electric double-layer. The cathodic and anodic current densities of L-Fe-NiCoLDH-2 at each scanning rate were greater than those of other catalysts, demonstrating improved double-layer discharge efficiency. The  $C_{dl}$  of L-Fe-NiCoLDH-2 was calculated to be 100 mF cm<sup>-2</sup>, which was larger than those of other catalysts (50, 94, and 29 mF cm<sup>-2</sup> for L-Fe-NiCoLDH-1, L-Fe-NiCoLDH-3, and L-NiCoLDH, respectively) (Figure 4d). The ECSA of the obtained electrolytes was linearly proportional to the double-layer capacitance ( $C_{dl}$ ) and specific capacitance ( $C_s$ ), where  $C_s$  is the specific capacitance and is generally taken as 22–130  $\mu$ F cm<sup>-2</sup> in KOH solution [59,60]. In this case, we employed  $C_s$  at a value of 40  $\mu$ F cm<sup>-2</sup>. As shown in Figure 4e, the L-Fe-NiCoLDH-2 exhibited larger ECSA than other catalysts, inducing its higher OER performance. Figure 4f shows the EIS data of the catalysts, analyzed from 100,000 Hz to 10 Hz. The charge transfer resistance ( $R_{ct}$ ), which reflected the rate of charge transfer, was calculated by fitting the original value on the Randles model. The charge transfer resistances of L-NiCoLDH, L-Fe-NiCoLDH-1, L-Fe-NiCoLDH-2, and Fe-NiCoLDH-3 were 28.1, 2.48, 1.53, and 4.29  $\Omega$ , respectively. The  $R_{ct}$  of L-Fe-NiCoLDH-2 was the smallest, suggesting a faster rate of charge transfer [36,61].

The stability of L-Fe-NiCoLDH-2 was investigated by cycling test and chronopotentiometry measurements (j-t). The cycling test (between 1.05 and 1.7 V vs. RHE) is a crucial benchmark for confirming durability. After 500 consecutive cycling tests, the catalyst exhibited a similar LSV curve, and variations in current density can be disregarded, as shown in Figure 5a. The charge transfer resistance value after durability test also shows similar results (Figure 5b). The stability of L-Fe-NiCoLDH-2 was compared with that of L-NiCo-LDH by performing chronopotentiometry measurements (j-t) at 10 mA cm<sup>-2</sup> for 20 h (see Figure 5c). During the stability test, it was observed that the overpotentials of the samples did not increase much. The LSV curve of L-Fe-NiCoLDH-2 showed an increase of 8 mV (3%) after 20 h, which was better than that of L-NiCoLDH (an increase of 17 mV after 20 h). In particular, the stability of L-Fe-NiCoLDH-2 was also conducted at a higher current density of 100 mA cm<sup>-2</sup> for 20 h (Figure 5d). The potential of L-Fe-NiCoLDH-2 was almost constant after 20 h during the test, indicating that the L-Fe-NiCoLDH-2 catalyst exhibited excellent catalytic activity and long-term stability. Furthermore, the morphology of L-Fe-NiCoLDH-2 remained after the long-term stability test (Figure S9). The XPS spectra of the L-Fe-NiCoLDH-2 electrode before and after the OER test was studied, as shown in Figure S10. After the OER test, the Ni 2p, Co 2p, and Fe 2p peaks shift to the positive, which

assigned to the oxidation of Ni, Co, and Fe on the catalyst surface during the catalytic process. However, the principal peaks of the elements were maintained, confirming the high stability of L-Fe-NiCoLDH-2.

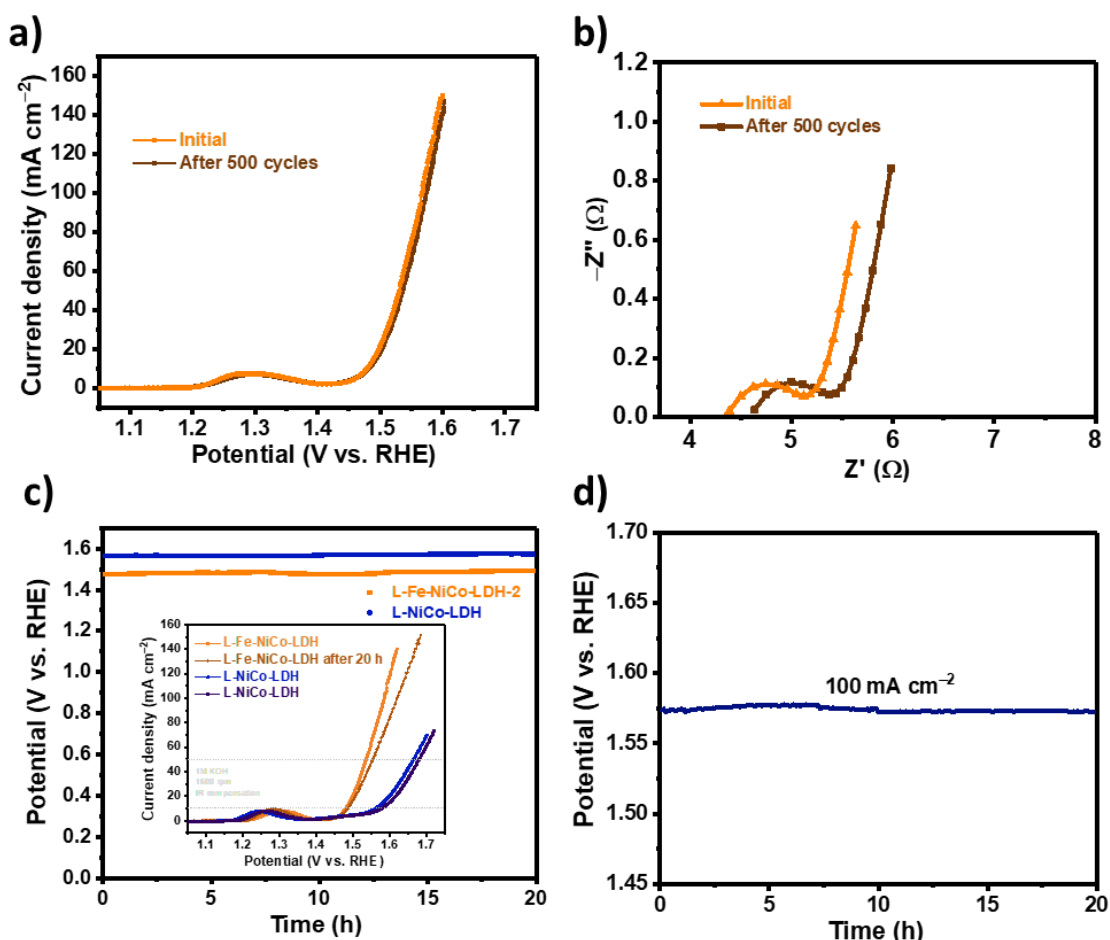


**Figure 5.** Electrocatalytic stability. (a,b) Polarization and EIS curves of L-Fe-NiCoLDH-2 electric catalyst initially as well as after 500 CV cycles. Long-term stability test of (c) L-Fe-NiCoLDH-2 and L-NiCoLDH at  $10 \text{ mA cm}^{-2}$  (inset LSV before and after 20 h), and (d) L-Fe-NiCoLDH-2 at  $100 \text{ mA cm}^{-2}$  for 20 h.

The OER in an alkaline solution involves four-electron transfer steps, as shown in Figure 6a. The metal–oxygen bond is an essential determinant of OER activity, including M–OH, M–O, M–OOH, and M–OO. Calculations using density functional theory identified the third step as the rate-determining phase since it had the largest Gibbs free energy [62]. By introducing Fe doping, the OER performance was improved owing to enhanced M–OOH active sites. The mechanisms of the OER process for L-NiCo-LDH and L-FeNiCo-LDH are described in Figure 6b,c, in which  $\text{Fe}^{3+}$  can replace  $\text{Ni}^{2+}$  and occupy the Ni position in the octahedral Ni (oxygen) hydroxide structure [63]. Therefore, it is possible to increase the valence state of nearby Ni positions, as indicated by the XPS results, suggesting that a  $\text{Ni}^{3+}$  state appears in L-FeNiCoLDH-2 but not in L-NiCoLDH. In addition, since the valence of Co does not change after Fe doping, it is assumed that only Ni species are affected by Fe doping. The generation of  $\text{Ni}^{3+}$  and  $\text{Fe}^{3+}$  results in the formation of active NiOOH and FeOOH species, which are the major active sites leading to higher OER performance. The leaf-shape morphology of the material also affects the OER performance. For comparison, we synthesized LDH materials by using the 3D morphology of ZIF-67 and compared the OER performances in Figure S11. As a result, the OER performance of materials from ZIFL represents the highest performance (Figure S12). The leaf morphology allows active sites to

be more exposed and makes the contact with electrons in the electrolyte easier than the 3D structure [64,65].

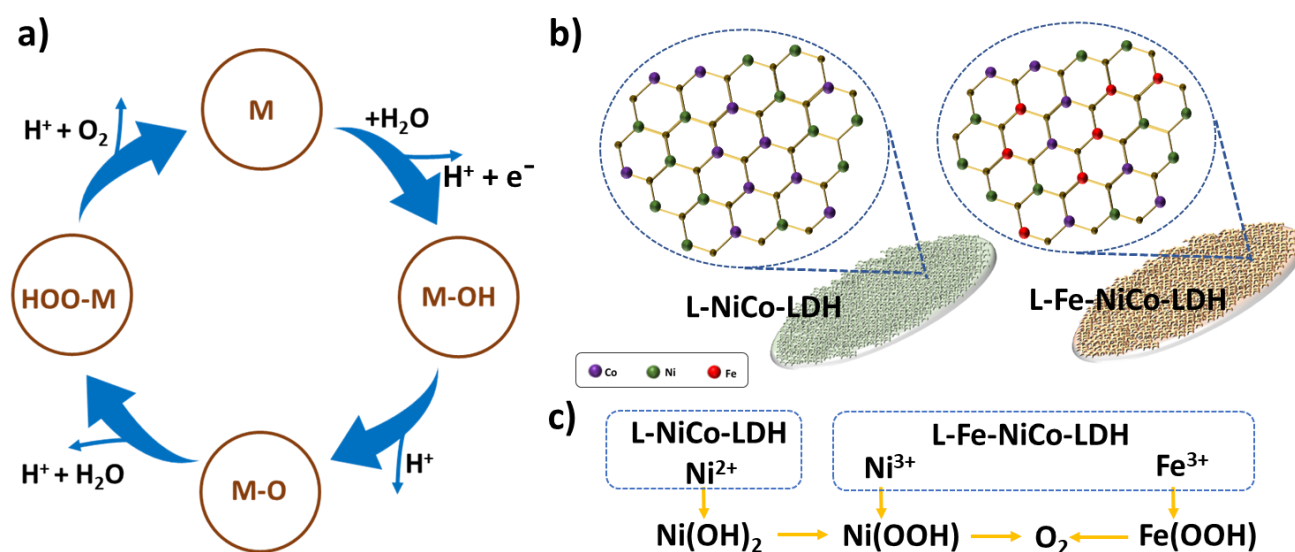


**Figure 6.** (a) Scheme for the OER process in alkaline media. M stands for Ni, Co, or Fe. (b) Schematic of the structure and (c) mechanism of L-NiCo-LDH and L-Fe-NiCo-LDH for enhanced OER performance.

### 3. Experimental Procedure

#### 3.1. Catalyst Preparation

First, 0.58 g of  $\text{Co}(\text{NO}_3)_2 \cdot 6\text{H}_2\text{O}$  (98%, Sigma-Aldrich, St. Louis, MO, USA) was dissolved in 40 mL of distilled water. Then, 1.3 g of 2-methylimidazole (98%, Sigma-Aldrich) dissolved in 40 mL DI water was dropped into the above solution. The mixed solution was stirred for 6 h at room temperature. The product was collected by centrifugation several times in water and dried at 70 °C, which was denoted as Co-ZIFL. Then, 0.16 g of Co-ZIFL was dispersed in the solution of 0.32 g  $\text{Ni}(\text{NO}_3)_2 \cdot 6\text{H}_2\text{O}$  (98%, Sigma-Aldrich) in 100 mL ethanol. The mixture was sonicated for 10 min for homogenous dispersion, followed by stirring for 30 min and washing, resulting in an LDH product, denoted as Co-ZIFL@NiCoLDH. To investigate the effect of Fe concentration, Co-ZIFL@NiCoLDH was dispersed in 50 mL ethanol containing various amounts of  $\text{Fe}(\text{NO}_3)_3$  (98%, Sigma-Aldrich) from 0.04 g to 0.08 g. Then, the mixture was refluxed at 90 °C for 1 h. During this time, the structure of ZIF was converted to an LDH structure, showing a color change from purple to brown. The final product was denoted as L-Fe-NiCoLDH-*x* (*x* = 1, 2, or 3 corresponding to 0.04, 0.06, and 0.08 g of  $\text{Fe}(\text{NO}_3)_3$ , respectively). L-NiCoLDH was also obtained by following the same method except for the addition of the Fe precursor.

For comparison, the hollow spheres ZIF 67 (S-ZIF 67) and particles ZIF 67 (P-ZIF 67) were synthesized. For synthesizing S-ZIF 67, 0.775 g  $\text{CoSO}_4 \cdot 7\text{H}_2\text{O}$  (99%, Sigma-Aldrich) was dispersed in 100 mL methanol. After that, 3.2 g 2-methylimidazole solution in 100 mL methanol was slowly added to the  $\text{CoSO}_4 \cdot 7\text{H}_2\text{O}$  and then mixed for 4 h under vigorous stirring to obtain a homogeneous system. Finally, S-ZIF 67 was collected after washing many times with methanol and water and dried at 70 °C. For synthesizing the P-ZIF 67, 0.582 g  $\text{Co}(\text{NO}_3)_2 \cdot 6\text{H}_2\text{O}$  was dispersed in 100 mL methanol. The 0.656 g 2-methylimidazole in 100 mL methanol was mixed with the previous solution and stirred 1 h at room temperature. The mixed solution was aged for 24 h. We synthesized 3D ZIF materials in particles and spherical shapes, which were denoted as P-ZIF-67 (ZIF-67 particles) and S-ZIF-67 (ZIF-67 spheres), respectively. The S-ZIF-67 and P-ZIF-67 were used for synthesizing S-Fe-NiCo-LDH and P-Fe-NiCo-LDH, respectively, with the similar procedure for synthesizing the L-Fe-NiCoLDH-2.

### 3.2. Structure Characterization

The crystal structures of all materials were obtained by X-ray diffraction (XRD, Cu K $\alpha$  ( $\lambda = 1.54 \text{ \AA}$ )). The morphology was measured by high-resolution field-emission scanning electron microscopy (HR FE-SEM; Merlin, Carl Zeiss, Gna, Germany) and field-emission transmission electron microscopy (FE-TEM; Talos F200X, FEL, Portland, OR, USA). The pore structure and the Brunauer–Emmett–Teller (BET) specific area were analyzed at 77 K with N<sub>2</sub> porosimetry (TRISTAR, Micromeritics, Norcross, GA, USA). X-ray photoelectron spectroscopy (XPS; K-alpha, Thermo Scientific, Waltham, MA, USA) was used to measure the oxidation state of each element. Most of the apparatus and equipment were supported by the Core Facility Center for Analysis of Optoelectronic Materials and Devices of the Korea Basic Science Institute (KBSI).

### 3.3. Electrochemical Measurement

All electrochemical measurements were measured in the workstation Auto-Lab (Metrohm, Herisau, Switzerland) using three-electrode systems. Glassy carbon (GC), Pt, and Ag/AgCl were used as the working, counter, and reference electrodes, respectively. Catalyst ink was prepared by mixing 5 mg of the catalyst with 1 mg of active carbon, 400  $\mu\text{L}$  isopropanol (IPA), and 30  $\mu\text{L}$  of Nafion solution (5 wt% Nafion in IPA). The catalyst ink was sonicated for 20 min for homogenous dispersion; then, 10  $\mu\text{L}$  of the catalyst ink was dropped in the GC electrode (0.196 cm<sup>2</sup>) and dried at room temperature. Linear sweep voltammetry (LSV) was conducted at a scan rate of 5 mV s<sup>-1</sup> in the potential range from 1.05 V to 1.7 V (vs. RHE) in 1.0 M KOH. Cycle voltammetry (CV) was performed in a nonfaradaic region at various scan rates (10, 20, 40, 60, 80, and 100 mV s<sup>-1</sup>) in the potential range from 1.3 V to 1.5 V to calculate the double-layer capacitance (C<sub>dl</sub>) and the electrochemically active surface area (ECSA). C<sub>dl</sub> was collected from the slope of the difference between anodic and cathodic current density in the middle of CV curves at various scan rates ( $\Delta j/2 = (j_a - j_c)/2$ ). Electrode impedance spectroscopy (EIS) was conducted in the frequency range from 100,000 Hz to 10 Hz to obtain R<sub>CT</sub> (charge transfer resistance). Long-term stability tests were executed at 10 and 100 mA cm<sup>-2</sup> for 20 h and cycling test for 500 cycles.

## 4. Conclusions

Hollow leaf-shaped L-Fe-NiCoLDH-x catalysts were synthesized for the oxygen evolution reaction. L-Fe-NiCoLDH-x was manufactured without calcination at high temperatures. As a result, the catalyst retained its 2D leaf morphology, maintaining the advantages of 2D materials for electrochemical catalysis. In addition, the formation rate of the LDH structure was increased by controlling the Fe concentration, further increasing the specific surface area and pore size. The L-FeNiCo-LDH-2 catalyst performed excellent OER performance in an alkaline electrolyte, showing an overpotential of 243 mV at 10 mA cm<sup>-2</sup>, a low Tafel slope of 63 mV dec<sup>-1</sup>, and high stability after 20 h. The catalyst's high performance was based on the improved ionic transport and electrical conductivity due to Fe doping. Based on the understanding of the LDH structure and OER activity, this study can pave the way for the fabrication of high-performance LDH materials derived from 2D MOFs for energy conversion, storage, and recycling.

**Supplementary Materials:** The following supporting information can be downloaded at: <https://www.mdpi.com/article/10.3390/catal13020403/s1>, Figure S1: (a,b) FE-SEM images of Co-ZIFL; Figure S2: Comparison of the XRD patterns of (a) Co-ZIFL and simulated Co-ZIFL patterns and (b) L-NiCoLDH and L-FeNiCoLDH-x; Figure S3: SEM images of (a,b) L-NiCoLDH (c,d) L-Fe-NiCoLDH-1, and (e,f) L-Fe-NiCoLDH-3 from Co-ZIFL; Figure S4: (a–d) FE-TEM image of L-NiCoLDH obtained from Co-ZIFL; Figure S5: EDX mapping of L-NiCoLDH obtained from Co-ZIFL; Figure S6: EDX signals of (a) L-NiCoLDH, (b) L-Fe-NiCoLDH-1, (c) L-Fe-NiCoLDH-2, and (d) L-Fe-NiCoLDH-3; Figure S7: XPS spectra of (I) L-NiCoLDH and (II) L-Fe-NiCoLDH-2; Figure S8: CV diagrams (a) L-NiCoLDH, (b) L-Fe-NiCoLDH-1, (c) L-Fe-NiCoLDH-2, and (d) L-Fe-NiCoLDH-3 in 1.0 M KOH within the range of 1.3–1.5 V vs. RHE at 10, 20, 40, 60, 80 and 100 mV s<sup>-1</sup>, respectively; Figure S9: FE-TEM image of L-Fe-NiCoLDH-2 after stability test; Figure S10: XPS data of L-Fe-NiCoLDH-2 after stability

test (a) XPS spectra, (b) Ni 2p (c) Co 2p, (d) Fe 2p; Figure S11: SEM images of (a,b) P-Fe-NiCoLDH from the P-ZIF-67, and (c,d) S-Fe-NiCoLDH from the S-ZIF-67; Figure S12: OER performance of P-Fe-NiCoLDH, S-Fe-NiCoLDH, and L-Fe-NiCoLDH; Table S1: Summary of the EDX elemental analysis of the catalysts; Table S2. Surface atomic concentrations of elements collected from the XPS spectra of L-Fe-NiCoLDH-2 and L-NiCoLDH.

**Author Contributions:** Conceptualization, Q.H.N. and K.I.; Methodology, Q.H.N. and K.I.; Validation, Q.H.N. and K.I.; Formal analysis, Q.H.N., K.I. and J.K.; Investigation, Q.H.N. and K.I.; Writing–Review and editing, Q.H.N., K.I. and J.K. Visualization, Q.H.N. and K.I.; Supervision, J.K.; Funding acquisition: J.K.; Funding: J.K. All authors have read and agreed to the published version of the manuscript.

**Funding:** This research was supported by the Basic Science Research Program (NRF-2019R1A2C1090693), and the Engineering Research Center of Excellence Program (NRF-2021R1A5A6002853) through the National Research Foundation of Korea (NRF), funded by the Ministry of Science and ICT, Republic of Korea.

**Data Availability Statement:** The data presented are available on request from the authors.

**Conflicts of Interest:** The authors declare no conflict of interest.

## References

1. Tahir, M.; Pan, L.; Idrees, F.; Zhang, X.; Wang, L.; Zou, J.J.; Wang, Z.L. Electrocatalytic Oxygen Evolution Reaction for Energy Conversion and Storage: A Comprehensive Review. *Nano Energy* **2017**, *37*, 136–157. [[CrossRef](#)]
2. Kalyanasundaram, K.; Grätzel, M. Themed Issue: Nanomaterials for Energy Conversion and Storage. *J. Mater. Chem.* **2012**, *22*, 24190–24194. [[CrossRef](#)]
3. Reddy, A.L.M.; Gowda, S.R.; Shaijumon, M.M.; Ajayan, P.M. Hybrid Nanostructures for Energy Storage Applications. *Adv. Mater.* **2012**, *24*, 5045–5064. [[CrossRef](#)]
4. Qu, K.; Zheng, Y.; Dai, S.; Qiao, S.Z. Graphene Oxide-Polydopamine Derived N, S-Codoped Carbon Nanosheets as Superior Bifunctional Electrocatalysts for Oxygen Reduction and Evolution. *Nano Energy* **2016**, *19*, 373–381. [[CrossRef](#)]
5. Ren, S.; Duan, X.; Liang, S.; Zhang, M.; Zheng, H. Bifunctional Electrocatalysts for Zn-Air Batteries: Recent Developments and Future Perspectives. *J. Mater. Chem. A* **2020**, *8*, 6144–6182. [[CrossRef](#)]
6. Hu, C.; Zhang, L.; Gong, J. Recent Progress Made in the Mechanism Comprehension and Design of Electrocatalysts for Alkaline Water Splitting. *Energy Environ. Sci.* **2019**, *12*, 2620–2645. [[CrossRef](#)]
7. Liu, X.; Yuan, Y.; Liu, J.; Liu, B.; Chen, X.; Ding, J.; Han, X.; Deng, Y.; Zhong, C.; Hu, W. Utilizing Solar Energy to Improve the Oxygen Evolution Reaction Kinetics in Zinc–Air Battery. *Nat. Commun.* **2019**, *10*, 4767. [[CrossRef](#)]
8. Bao, W.; Yang, C.; Ai, T.; Zhang, J.; Zhou, L.; Li, Y.; Wei, X.; Zou, X.; Wang, Y. Modulating Interfacial Charge Distribution of NiSe Nanoarrays with NiFe-LDH Nanosheets for Boosting Oxygen Evolution Reaction. *Fuel* **2023**, *332*, 126227. [[CrossRef](#)]
9. Simböck, J.; Ghiasi, M.; Schönebaum, S.; Simon, U.; de Groot, F.M.F.; Palkovits, R. Electronic Parameters in Cobalt-Based Perovskite-Type Oxides as Descriptors for Chemocatalytic Reactions. *Nat. Commun.* **2020**, *11*, 652. [[CrossRef](#)]
10. Fabbri, E.; Nachttegaal, M.; Binninger, T.; Cheng, X.; Kim, B.J.; Durst, J.; Bozza, F.; Graule, T.; Schäublin, R.; Wiles, L.; et al. Dynamic Surface Self-Reconstruction Is the Key of Highly Active Perovskite Nano-Electrocatalysts for Water Splitting. *Nat. Mater.* **2017**, *16*, 925–931. [[CrossRef](#)]
11. Zhang, Z.; Sun, H.; Li, J.; Shi, Z.; Fan, M.; Bian, H.; Wang, T.; Gao, D. S-Doped CoMn<sub>2</sub>O<sub>4</sub> with More High Valence Metallic Cations and Oxygen Defects for Zinc-Air Batteries. *J. Power Source* **2021**, *491*, 229584. [[CrossRef](#)]
12. Gao, L.; Cui, X.; Wang, Z.; Sewell, C.D.; Li, Z.; Liang, S.; Zhang, M.; Li, J.; Hu, Y.; Lin, Z. Operando Unraveling Photothermal-Promoted Dynamic Active-Sites Generation in NiFe<sub>2</sub>O<sub>4</sub> for Markedly Enhanced Oxygen Evolution. *Proc. Natl. Acad. Sci. USA* **2021**, *118*, e2023421118. [[CrossRef](#)] [[PubMed](#)]
13. Bothra, P.; Pati, S.K. Activity of Water Oxidation on Pure and (Fe, Ni, and Cu)-Substituted Co<sub>3</sub>O<sub>4</sub>. *ACS Energy Lett.* **2016**, *1*, 858–862. [[CrossRef](#)]
14. Dionigi, F.; Zeng, Z.; Sinev, I.; Merzdorf, T.; Deshpande, S.; Lopez, M.B.; Kunze, S.; Zegkinoglou, I.; Sarodnik, H.; Fan, D.; et al. In-Situ Structure and Catalytic Mechanism of NiFe and CoFe Layered Double Hydroxides during Oxygen Evolution. *Nat. Commun.* **2020**, *11*, 2522. [[CrossRef](#)] [[PubMed](#)]
15. Chen, R.; Hung, S.F.; Zhou, D.; Gao, J.; Yang, C.; Tao, H.; Bin Yang, H.; Zhang, L.; Zhang, L.; Xiong, Q.; et al. Layered Structure Causes Bulk NiFe Layered Double Hydroxide Unstable in Alkaline Oxygen Evolution Reaction. *Adv. Mater.* **2019**, *31*, e1903909. [[CrossRef](#)]
16. Liu, G.; Ouyang, X.; Wei, X.L.; Bao, W.W.; Feng, X.H.; Zhang, J.J. Coupling Interface Construction of Ni(OH)<sub>2</sub>/MoS<sub>2</sub> Composite Electrode for Efficient Alkaline Oxygen Evolution Reaction. *Catalysts* **2022**, *12*, 966. [[CrossRef](#)]
17. Zhang, J.J.; Li, M.Y.; Li, X.; Bao, W.W.; Jin, C.Q.; Feng, X.H.; Liu, G.; Yang, C.M.; Zhang, N.N. Chromium-Modified Ultrathin CoFe LDH as High-Efficiency Electrode for Hydrogen Evolution Reaction. *Nanomaterials* **2022**, *12*, 1227. [[CrossRef](#)]

18. Han, L.; Dong, S.; Wang, E. Transition-Metal Co Ni and Fe-Based Electrocatalysts for the Water Oxidation Reaction. *Adv. Mater.* **2016**, *28*, 9266–9291. [[CrossRef](#)]
19. Ma, Q.; Li, B.; Huang, F.; Pang, Q.; Chen, Y.; Zhang, J.Z. Incorporating Iron in Nickel Cobalt Layered Double Hydroxide Nanosheet Arrays as Efficient Oxygen Evolution Electrocatalyst. *Electrochim. Acta* **2019**, *317*, 684–693. [[CrossRef](#)]
20. Li, N.; Bediako, D.K.; Hadt, R.G.; Hayes, D.; Kempa, T.J.; Von Cube, F.; Bell, D.C.; Chen, L.X.; Nocera, D.G. Influence of Iron Doping on Tetravalent Nickel Content in Catalytic Oxygen Evolving Films. *Proc. Natl. Acad. Sci. USA* **2017**, *114*, 1486–1491. [[CrossRef](#)]
21. Chung, D.Y.; Lopes, P.P.; Farinazzo Bergamo Dias Martins, P.; He, H.; Kawaguchi, T.; Zapol, P.; You, H.; Tripkovic, D.; Strmcnik, D.; Zhu, Y.; et al. Dynamic Stability of Active Sites in Hydr(Oxy)Oxides for the Oxygen Evolution Reaction. *Nat. Energy* **2020**, *5*, 220–230. [[CrossRef](#)]
22. Nguyen, Q.H.; Im, K.; Kim, J. Synthesis of Hollow Fe, Co, and N-Doped Carbon Catalysts from Conducting Polymer-Metal-Organic-Frameworks Core-Shell Particles for Their Application in an Oxygen Reduction Reaction. *Int. J. Hydrogen Energy* **2022**, *47*, 24169–24178. [[CrossRef](#)]
23. Zhang, C.; Yang, H.; Zhong, D.; Xu, Y.; Wang, Y.; Yuan, Q.; Liang, Z.; Wang, B.; Zhang, W.; Zheng, H.; et al. A Yolk-Shell Structured Metal-Organic Framework with Encapsulated Iron-Porphyrin and Its Derived Bimetallic Nitrogen-Doped Porous Carbon for an Efficient Oxygen Reduction Reaction. *J. Mater. Chem. A* **2020**, *8*, 9536–9544. [[CrossRef](#)]
24. Wang, H.F.; Chen, L.; Pang, H.; Kaskel, S.; Xu, Q. MOF-Derived Electrocatalysts for Oxygen Reduction, Oxygen Evolution and Hydrogen Evolution Reactions. *Chem. Soc. Rev.* **2020**, *49*, 1414–1448. [[CrossRef](#)] [[PubMed](#)]
25. Song, Z.; Cheng, N.; Lushington, A.; Sun, X. Recent Progress on MOF-Derived Nanomaterials as Advanced Electrocatalysts in Fuel Cells. *Catalysts* **2016**, *6*, 116. [[CrossRef](#)]
26. Zhang, Y.; Qi, L. MOF-Derived Nanoarrays as Advanced Electrocatalysts for Water Splitting. *Nanoscale* **2022**, *14*, 12196–12218. [[CrossRef](#)]
27. Duan, X.; Ren, S.; Pan, N.; Zhang, M.; Zheng, H. MOF-Derived Fe,Co@N-C Bifunctional Oxygen Electrocatalysts for Zn-Air Batteries. *J. Mater. Chem. A* **2020**, *8*, 9355–9363. [[CrossRef](#)]
28. Jiang, K.; Luo, M.; Peng, M.; Yu, Y.; Lu, Y.R.; Chan, T.S.; Liu, P.; de Groot, F.M.F.; Tan, Y. Dynamic Active-Site Generation of Atomic Iridium Stabilized on Nanoporous Metal Phosphides for Water Oxidation. *Nat. Commun.* **2020**, *11*, 2701. [[CrossRef](#)]
29. Zhang, J.; Sun, X.; Liu, Y.; Hou, L.; Yuan, C. Design and Construction of Bi-Metal MOF-Derived Yolk-Shell Ni<sub>2</sub>P/ZnP<sub>2</sub> Hollow Microspheres for Efficient Electrocatalytic Oxygen Evolution. *Mater. Chem. Front.* **2020**, *4*, 1366–1374. [[CrossRef](#)]
30. Chen, C.; Tuo, Y.; Lu, Q.; Lu, H.; Zhang, S.; Zhou, Y.; Zhang, J.; Liu, Z.; Kang, Z.; Feng, X.; et al. Hierarchical Trimetallic Co-Ni-Fe Oxides Derived from Core-Shell Structured Metal-Organic Frameworks for Highly Efficient Oxygen Evolution Reaction. *Appl. Catal. B Environ.* **2021**, *287*, 119953. [[CrossRef](#)]
31. Zhang, P.; Li, L.; Nordlund, D.; Chen, H.; Fan, L.; Zhang, B.; Sheng, X.; Daniel, Q.; Sun, L. Dendritic Core-Shell Nickel-Iron-Copper Metal/Metal Oxide Electrode for Efficient Electrocatalytic Water Oxidation. *Nat. Commun.* **2018**, *9*, 381. [[CrossRef](#)] [[PubMed](#)]
32. Zhang, J.; Yu, L.; Chen, Y.; Lu, X.F.; Gao, S.; Lou, X.W. Designed Formation of Double-Shelled Ni-Fe Layered-Double-Hydroxide Nanocages for Efficient Oxygen Evolution Reaction. *Adv. Mater.* **2020**, *32*, 1906432. [[CrossRef](#)] [[PubMed](#)]
33. Li, J.G.; Sun, H.; Lv, L.; Li, Z.; Ao, X.; Xu, C.; Li, Y.; Wang, C. Metal-Organic Framework-Derived Hierarchical (Co,Ni)Se<sub>2</sub>@NiFe LDH Hollow Nanocages for Enhanced Oxygen Evolution. *ACS Appl. Mater. Interfaces* **2019**, *11*, 8106–8114. [[CrossRef](#)] [[PubMed](#)]
34. Huang, L.; Zhang, X.; Han, Y.; Wang, Q.; Fang, Y.; Dong, S. In Situ Synthesis of Ultrathin Metal-Organic Framework Nanosheets: A New Method for 2D Metal-Based Nanoporous Carbon Electrocatalysts. *J. Mater. Chem. A* **2017**, *5*, 18610–18617. [[CrossRef](#)]
35. Duan, J.; Chen, S.; Zhao, C. Ultrathin Metal-Organic Framework Array for Efficient Electrocatalytic Water Splitting. *Nat. Commun.* **2017**, *8*, 15341. [[CrossRef](#)]
36. Yilmaz, G.; Yam, K.M.; Zhang, C.; Fan, H.J.; Ho, G.W. In Situ Transformation of MOFs into Layered Double Hydroxide Embedded Metal Sulfides for Improved Electrocatalytic and Supercapacitive Performance. *Adv. Mater.* **2017**, *29*, 1606814. [[CrossRef](#)]
37. He, P.; Yu, X.Y.; Lou, X.W.D. Carbon-Incorporated Nickel-Cobalt Mixed Metal Phosphide Nanoboxes with Enhanced Electrocatalytic Activity for Oxygen Evolution. *Angew. Chem.-Int. Ed.* **2017**, *56*, 3897–3900. [[CrossRef](#)]
38. Wang, T.; Zhang, S.; Yan, X.; Lyu, M.; Wang, L.; Bell, J.; Wang, H. 2-Methylimidazole-Derived Ni-Co Layered Double Hydroxide Nanosheets as High Rate Capability and High Energy Density Storage Material in Hybrid Supercapacitors. *ACS Appl. Mater. Interfaces* **2017**, *9*, 15510–15524. [[CrossRef](#)]
39. Naseem, S.; Gevers, B.; Boldt, R.; Labuschagné, F.J.W.J.; Leuteritz, A. Comparison of Transition Metal (Fe, Co, Ni, Cu, and Zn) Containing Tri-Metal Layered Double Hydroxides (LDHs) Prepared by Urea Hydrolysis. *RSC Adv.* **2019**, *9*, 3030–3040. [[CrossRef](#)]
40. Cheng, M.; Fan, H.; Song, Y.; Cui, Y.; Wang, R. Interconnected Hierarchical NiCo<sub>2</sub>O<sub>4</sub> Microspheres as High-Performance Electrode Materials for Supercapacitors. *Dalt. Trans.* **2017**, *46*, 9201–9209. [[CrossRef](#)]
41. Wang, H.Y.; Hsu, Y.Y.; Chen, R.; Chan, T.S.; Chen, H.M.; Liu, B. Ni<sup>3+</sup>-Induced Formation of Active NiOOH on the Spinel Ni-Co Oxide Surface for Efficient Oxygen Evolution Reaction. *Adv. Energy Mater.* **2015**, *5*, 1500091. [[CrossRef](#)]
42. Ao, K.; Dong, J.; Fan, C.; Wang, D.; Cai, Y.; Li, D.; Huang, F.; Wei, Q. Formation of Yolk-Shelled Nickel-Cobalt Selenide Dodecahedral Nanocages from Metal-Organic Frameworks for Efficient Hydrogen and Oxygen Evolution. *ACS Sustain. Chem. Eng.* **2018**, *6*, 10952–10959. [[CrossRef](#)]
43. Chen, W.; Zhang, Y.; Huang, R.; Zhou, Y.; Wu, Y.; Hu, Y.; Ostrikov, K.K. Ni-Co Hydroxide Nanosheets on Plasma-Reduced Co-Based Metal-Organic Nanocages for Electrocatalytic Water Oxidation. *J. Mater. Chem. A* **2019**, *7*, 4950–4959. [[CrossRef](#)]

44. Zhou, Q.; Chen, Y.; Zhao, G.; Lin, Y.; Yu, Z.; Xu, X.; Wang, X.; Liu, H.K.; Sun, W.; Dou, S.X. Active-Site-Enriched Iron-Doped Nickel/Cobalt Hydroxide Nanosheets for Enhanced Oxygen Evolution Reaction. *ACS Catal.* **2018**, *8*, 5382–5390. [[CrossRef](#)]
45. Dutta, S.; Indra, A.; Feng, Y.; Song, T.; Paik, U. Self-Supported Nickel Iron Layered Double Hydroxide-Nickel Selenide Electrocatalyst for Superior Water Splitting Activity. *ACS Appl. Mater. Interfaces* **2017**, *9*, 33766–33774. [[CrossRef](#)] [[PubMed](#)]
46. Han, Y.; Li, P.; Liu, J.; Wu, S.; Ye, Y.; Tian, Z.; Liang, C. Strong Fe<sup>3+</sup>-O(H)-Pt Interfacial Interaction Induced Excellent Stability of Pt/NiFe-LDH/RGO Electrocatalysts. *Sci. Rep.* **2018**, *8*, 2–10. [[CrossRef](#)] [[PubMed](#)]
47. Ramachandran, R.; Lan, Y.; Xu, Z.X.; Wang, F. Construction of NiCo-Layered Double Hydroxide Microspheres from Ni-MOFs for High-Performance Asymmetric Supercapacitors. *ACS Appl. Energy Mater.* **2020**, *3*, 6633–6643. [[CrossRef](#)]
48. Guan, C.; Liu, X.; Ren, W.; Li, X.; Cheng, C.; Wang, J. Rational Design of Metal-Organic Framework Derived Hollow NiCo<sub>2</sub>O<sub>4</sub> Arrays for Flexible Supercapacitor and Electrocatalysis. *Adv. Energy Mater.* **2017**, *7*, 1602391. [[CrossRef](#)]
49. Zhou, D.; Li, P.; Lin, X.; McKinley, A.; Kuang, Y.; Liu, W.; Lin, W.F.; Sun, X.; Duan, X. Layered Double Hydroxide-Based Electrocatalysts for the Oxygen Evolution Reaction: Identification and Tailoring of Active Sites, and Superaerophobic Nanoarray Electrode Assembly. *Chem. Soc. Rev.* **2021**, *50*, 8790–8817. [[CrossRef](#)]
50. Wang, H.Y.; Hung, S.F.; Chen, H.Y.; Chan, T.S.; Chen, H.M.; Liu, B. In Operando Identification of Geometrical-Site-Dependent Water Oxidation Activity of Spinell Co<sub>3</sub>O<sub>4</sub>. *J. Am. Chem. Soc.* **2016**, *138*, 36–39. [[CrossRef](#)]
51. Septiani, N.L.W.; Kaneti, Y.V.; Guo, Y.; Yulianto, B.; Jiang, X.; Ide, Y.; Nugraha, N.; Dipojono, H.K.; Yu, A.; Sugahara, Y.; et al. Holey Assembly of Two-Dimensional Iron-Doped Nickel-Cobalt Layered Double Hydroxide Nanosheets for Energy Conversion Application. *ChemSusChem* **2020**, *13*, 1645–1655. [[CrossRef](#)] [[PubMed](#)]
52. Zhou, P.; Wang, Y.; Xie, C.; Chen, C.; Liu, H.; Chen, R.; Huo, J.; Wang, S. Acid-Etched Layered Double Hydroxides with Rich Defects for Enhancing the Oxygen Evolution Reaction. *Chem. Commun.* **2017**, *53*, 11778–11781. [[CrossRef](#)] [[PubMed](#)]
53. Bao, J.; Xie, J.; Lei, F.; Wang, Z.; Liu, W.; Xu, L.; Guan, M.; Zhao, Y.; Li, H. Two-Dimensional Mn-Co LDH/Graphene Composite towards High-Performance Water Splitting. *Catalysts* **2018**, *8*, 350. [[CrossRef](#)]
54. Wang, C.; Shang, H.; Li, J.; Wang, Y.; Xu, H.; Wang, C.; Guo, J.; Du, Y. Ultralow Ru Doping Induced Interface Engineering in MOF Derived Ruthenium-Cobalt Oxide Hollow Nanobox for Efficient Water Oxidation Electrocatalysis. *Chem. Eng. J.* **2021**, *420*, 129805. [[CrossRef](#)]
55. Yang, M.; Zhu, W.; Zhao, R.; Wang, H.; Ye, T.N.; Liu, Y.; Yan, D. MOF-Derived Hollow Spherical Co<sub>2</sub>P@C Composite with Micro-Nanostructure for Highly Efficient Oxygen Evolution Reaction in Alkaline Solution. *J. Solid State Chem.* **2020**, *288*, 121456. [[CrossRef](#)]
56. Cheng, W.; Xi, S.; Wu, Z.P.; Luan, D.; Lou, X.W. In Situ Activation of Br-Confined Ni-Based Metal-Organic Framework Hollow Prisms toward Efficient Electrochemical Oxygen Evolution. *Sci. Adv.* **2021**, *7*, eabk0919. [[CrossRef](#)]
57. Rinawati, M.; Wang, Y.X.; Chen, K.Y.; Yeh, M.H. Designing a Spontaneously Deriving NiFe-LDH from Bimetallic MOF-74 as an Electrocatalyst for Oxygen Evolution Reaction in Alkaline Solution. *Chem. Eng. J.* **2021**, *423*, 130204. [[CrossRef](#)]
58. Baumann, A.E.; Burns, D.A.; Liu, B.; Thoi, V.S. Metal-Organic Framework Functionalization and Design Strategies for Advanced Electrochemical Energy Storage Devices. *Commun. Chem.* **2019**, *2*, 86. [[CrossRef](#)]
59. McCrory, C.C.L.; Jung, S.; Peters, J.C.; Jaramillo, T.F. Benchmarking Heterogeneous Electrocatalysts for the Oxygen Evolution Reaction. *J. Am. Chem. Soc.* **2013**, *135*, 16977–16987. [[CrossRef](#)]
60. Lin, Y.; Tian, Z.; Zhang, L.; Ma, J.; Jiang, Z.; Deibert, B.J.; Ge, R.; Chen, L. Chromium-Ruthenium Oxide Solid Solution Electrocatalyst for Highly Efficient Oxygen Evolution Reaction in Acidic Media. *Nat. Commun.* **2019**, *10*, 162. [[CrossRef](#)]
61. Liang, Z.; Qu, C.; Zhou, W.; Zhao, R.; Zhang, H.; Zhu, B.; Guo, W.; Meng, W.; Wu, Y.; Aftab, W.; et al. Synergistic Effect of Co-Ni Hybrid Phosphide Nanocages for Ultrahigh Capacity Fast Energy Storage. *Adv. Sci.* **2019**, *6*, 1802005. [[CrossRef](#)] [[PubMed](#)]
62. Zhang, J.; Liu, J.; Xi, L.; Yu, Y.; Chen, N.; Sun, S.; Wang, W.; Lange, K.M.; Zhang, B. Single-Atom Au/NiFe Layered Double Hydroxide Electrocatalyst: Probing the Origin of Activity for Oxygen Evolution Reaction. *J. Am. Chem. Soc.* **2018**, *140*, 3876–3879. [[CrossRef](#)] [[PubMed](#)]
63. Burke, M.S.; Enman, L.J.; Batchelor, A.S.; Zou, S.; Boettcher, S.W. Oxygen Evolution Reaction Electrocatalysis on Transition Metal Oxides and (Oxy)Hydroxides: Activity Trends and Design Principles. *Chem. Mater.* **2015**, *27*, 7549–7558. [[CrossRef](#)]
64. Dhakshinamoorthy, A.; Asiri, A.M.; Garcia, H. 2D Metal-Organic Frameworks as Multifunctional Materials in Heterogeneous Catalysis and Electro/Photocatalysis. *Adv. Mater.* **2019**, *31*, e1900617. [[CrossRef](#)] [[PubMed](#)]
65. Im, K.; Nguyen, Q.H.; Lee, E.; Lee, D.W.; Kim, J.; Yoo, S.J. High-Dispersion Co-Fe-NC Electrocatalyst Based on Leaf-Shaped Zeolite Imidazole Framework for Oxygen-Reduction Reaction in Acidic Medium. *Int. J. Energy Res.* **2021**, *45*, 15534–15543. [[CrossRef](#)]

**Disclaimer/Publisher's Note:** The statements, opinions and data contained in all publications are solely those of the individual author(s) and contributor(s) and not of MDPI and/or the editor(s). MDPI and/or the editor(s) disclaim responsibility for any injury to people or property resulting from any ideas, methods, instructions or products referred to in the content.